

## THERMAL MANAGEMENT

# Mesoporous optically clear heat insulators for sustainable building envelopes

Amit Bhardwaj<sup>1†</sup>, Blaise Fleury<sup>1†</sup>, Bohdan Senyuk<sup>1,2†</sup>, Eldho Abraham<sup>1,2†</sup>, Jan Bart ten Hove<sup>1†</sup>, Taewoo Lee<sup>1,2†</sup>, Vladyslav Cherpak<sup>1†</sup>, Ivan I. Smalyukh<sup>1,2,3,4\*</sup>

Mesoporous materials exhibit highly controlled nanoscale structures, often templated by liquid crystalline assemblies of surfactants, with emergent and often designable physical properties. However, scaling their fabrication to be suitable for uses such as envelopes of buildings is challenging. In this work, we describe fabrication of flexible square-meter-sized films and multicentimeter-thick slabs made of three-dimensional spatial graphs of mesopore tubes that have all structural features under 50 nanometers. A solution-based kinetic fabrication process templates growing networks of cylindrical surfactant micelles with thin tubes of polysiloxane-forming gel networks and, upon replacing surfactants and solvents with air, yields lightweight materials with greater than 99% visible-range optical transparency and approximately 10 milliwatts per kelvin per meter thermal conductivity. Such predesigned metamaterials enable transparent thermal barriers for wall-grade insulated glass units, square-meter window retrofits, and unconcentrated solar thermal energy harnessing.

Buildings are responsible for consuming ~40% of all generated energy globally, and much of that energy is wasted in heating and cooling the building interior (1–7) because building envelopes commonly lack the ability to passively maintain the temperature needed for a comfortable indoor environment. Windows of buildings leak much of the cooling and heating energy (2–5): Despite constituting on average only ~8% (often ~30% in modern high-end homes) by area of the building envelopes, they are responsible for ~50% of the heat transfer (2–5). Approaches that aim to address this challenge involve transparent cellulose or silica aerogels and vacuum-insulated glass units, but their deployment is still challenged by issues such as scaling limitations, seal integrity, and high manufacturing costs (2–14). Recently, cellulose-based aerogel films could be scaled in lateral dimensions while achieving optical characteristics acceptable for window retrofitting applications (11), although their thickness could not be scaled beyond several millimeters while retaining transparency, which limits the overall thermal resistance that could be achieved in window units and retrofits. The high nanometers-to-micrometer polydispersity of pores in conventional aerogels is the primary contributor to their hazy appearance, making it difficult for aerogels to meet the stringent optical requirements for applications in windows (7–14), as well as making them less effective as thermal barriers (15, 16). Despite the recent progress in meticulous nanoscale morphology control (3–14), the intrinsic limitations of conventional aerogels stem from the lack of well-defined length-scale controlling pores to stay much smaller than both

the wavelength of light and mean free path of air molecules at ambient conditions (~60 nm), which is needed to achieve high optical transparency and low thermal conductivity in porous materials (4).

Mesoporous materials, including mesoporous silicas, have been developed to exhibit highly controlled monodisperse pores, which are often templated by means of lyotropic liquid crystalline mesophases or kinetic processes that involve mesoscale self-organization of micelles (17–23). However, such materials have not been reported to be manufactured on building-relevant scales. Similarly, the target physical properties such as thermal insulation and optical transparency have not been systematically studied or optimized.

We report optically transparent, highly thermally insulating preengineered metamaterials made from mesopore networks of polysiloxane tubes as a viable alternative for window insulation (24). By tuning mesoscale structure and solid content, we achieved thermal conductivity of 10 to 12 mW K<sup>-1</sup> m<sup>-1</sup>, which is much lower than that of still air (~27 mW K<sup>-1</sup> m<sup>-1</sup>), as well as average visible-range light transmission >99% (much higher than <92% of glass) with a haze coefficient <1%. We scaled production of these mesoporous optically clear heat insulators (MOCHIs) to square-meter lateral dimensions and slab thicknesses >3 cm, to overall building-relevant scales, while retaining their thermal and optical properties. We fabricated wall-grade insulated glass units with thermal resistance  $R \approx 2.64 \text{ m}^2 \text{ K W}^{-1}$  (15 foot<sup>2</sup>-hours °F Btu<sup>-1</sup>) and greater for geometric form factors (thickness) comparable with that of conventional double-pane windows, while also meeting stringent requirements for such glazing applications. Additionally, we demonstrated how such transparent insulation allows for efficient harnessing of unconcentrated solar thermal energy. MOCHI metamaterials could potentially help convert inefficient building envelopes into energy-generating autonomous power plants.

## Fabrication of slabs and films of MOCHI metamaterials

By using an optimized procedure that leveraged the out-of-equilibrium self-assembly of surfactant molecules into graph-like networks, which then templated networks of thin nanotubes of polysiloxane to eventually yield our predesigned MOCHI metamaterials (Fig. 1, C to J, and figs. S1 and S2), we fabricated square-meter films and multicentimeter-thick slabs (Fig. 1, A and B; figs. S3 and S4; and movies S1 and S2). Briefly, methyl trimethoxy silane (MTMS) was added to a solution of an aqueous cetylpyridinium chloride (CPCL) surfactant, followed by additions of glacial acetic acid to hydrolyze the silane. Tetramethyl ethylene diamine (TEMED) was used to cross-link the polysiloxane network (tables S1 and S2) (24). This mixture was transferred to a prefabricated mold, which was sealed and then kept in a closed chamber to complete gelation at 55°C within 12 to 72 hours, for sample thicknesses of 0.5 to 37.5 mm, respectively (24). After removal from the mold, the polysiloxane hydrogels were washed with water and transferred to ethanol at 40°C. Repeated washing with fresh or distilled ethanol completed the solvent exchange and removed the surfactant (24). Subsequent carbon dioxide (CO<sub>2</sub>)-based supercritical drying replaced ethanol with CO<sub>2</sub> that was then exchanged with air within the mesoporous tubular networks after removal by use of a custom-built supercritical dryer (fig. S3F). The ensuing highly porous MOCHI metamaterials were predesigned to have a polysiloxane solid content of only 5 to 15% by volume (Fig. 1 and fig. S5), fabricated according to recipes shown in tables S1 and S2 (24).

Transmission electron microscopy (TEM) imaging and tomographic reconstruction (Fig. 1, C to F; fig. S1; and movies S3 and S4) confirmed that MOCHIs were composed of graph-like networks of thin bicontinuous tubes of polysiloxane. The inner pore diameters were roughly twice the length of CPCL surfactant molecules, and their nanometer-scale thickness and density varied with porosity (Fig. 1, C to I) (24). Dimensions of outer internanotube network pores were typically ~30 nm or less. The nanotube orientations exhibited weak orientational correlations with respect to the geometry of the slabs or films that was related

<sup>1</sup>Department of Physics, University of Colorado Boulder, Boulder, CO, USA. <sup>2</sup>International Institute for Sustainability with Knotted Chiral Meta Matter (WPI-SKCM<sup>2</sup>), Hiroshima University, Higashi-Hiroshima, Hiroshima, Japan. <sup>3</sup>Materials Science and Engineering Program, University of Colorado Boulder, Boulder, CO, USA. <sup>4</sup>Renewable and Sustainable Energy Institute, National Renewable Energy Laboratory and University of Colorado Boulder, Boulder, CO, USA. \*Corresponding author. Email: ivan.smalyukh@colorado.edu  
†These authors contributed equally to this work.

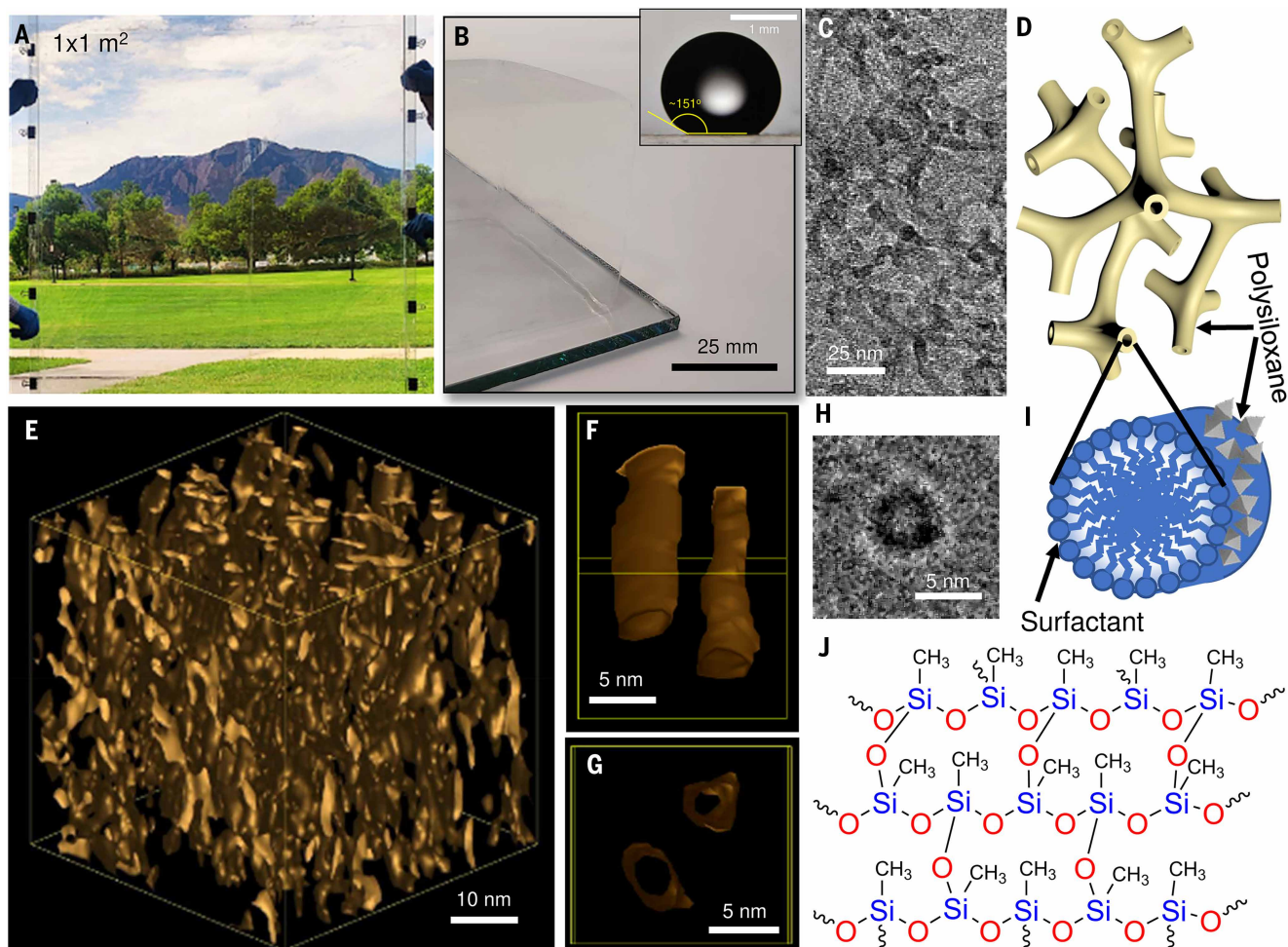


**Fig. 1. Large-scale MOCHI metamaterials and their nanoscale morphology.** (A) Optical photograph illustrating high transparency of a square-meter retrofit with 3-mm-thick MOCHI atop a plastic film. (B) A corner perspective view of a 5-cm-thick highly transparent MOCHI slab atop a glass plate. (Inset) A water droplet atop of MOCHI, with a large contact angle highlighting superhydrophobicity (24). (C) TEM image of a MOCHI, revealing the graph-like networks. (D) Corresponding schematic illustration of the nanotube graph network. (E) TEM tomographic reconstruction of the nanoscale morphology of MOCHI, demonstrating the orientationally orderly arrangement of hollow polysiloxane tubes within a graph-like network. (F and G) Zoomed-in tomographic reconstructions of two individual nanotubes viewed from mutually orthogonal perspectives. (H) TEM image of an edge-on-oriented polysiloxane tube templated by a cylindrical micelle of surfactant molecules, as shown in (I) the schematic. (J) Polysiloxane network within the walls of nanotubes.

to the symmetry-breaking at the fabrication-stage solvent exchange and drying (24).

The morphology of MOCHIs (Fig. 1D) is much different from that of common aerogels that are typically composed of networks of interconnected particles such as nanospheres and nanofibers with polydisperse pore dimensions that span many orders of magnitude (4–11), often from nanometers to tens of micrometers. Controlling pore and nanoparticle dimensions in nanocellulose and silica aerogels has been instrumental for achieving desired properties (4–11) such as optical transparency. However, progress has been limited, and so far, thick slabs of transparent aerogels have not been reported. By exploiting the surfactant self-assembly into cylindrical micellar networks as a guiding mechanism for nanotemplating polysiloxane, we define dimensions of inner pores of nanotubes, distances between them within the graph-like networks, as well as their large-scale partial orientational order and anisotropic properties (Figs. 1 and 2).

### Optical, thermal, and other properties

Our MOCHI metamaterials were highly transparent (Figs. 1, A and B, and 2; figs. S6 to S9; and movies S5 to S8), effectively behaving like “frozen air,” in contrast to hazy conventional aerogels that are often referred

to as “frozen smoke.” In Fig. 2B, we illustrate the dramatic differences between transmission of light incident obliquely on edge faces of MOCHIs and conventional window glass, in which glass is nontransparent for large incidence angles owing to the large contrast between refractive indices of glass (1.52) and air (1.0003). Because the refractive index of MOCHIs (1.025 to 1.030) nearly matched that of air, MOCHIs remained highly transparent even at large incidence angles (Fig. 2, A to D). The very small  $<0.03$  difference between the indices of air and MOCHIs as compared with that of glass ( $>0.5$ ) also caused the net total measured reflection from two MOCHI-air interfaces to be  $\approx 0.02\%$ , which is much lower than the corresponding  $\sim 8\%$  reflectivity value for a slab of glass (Fig. 2D, inset).

Furthermore, even the very low reflection from air-MOCHI interfaces disappeared when two slabs of MOCHI were pressed against each other to achieve optical contact (Fig. 2, E and F, and movie S2), which was easier to achieve than with glass because of the comparatively soft nature of MOCHIs. As a result,  $>99\%$  of normally incident visible light was transmitted, with  $\approx 99.7\%$  visible-range transmission measured with the help of an integrating sphere (24). Transmittance remained high ( $>90\%$ ) even for incidence angles  $>70^\circ$  and over the entire visible spectrum (Fig. 2, B and F, and fig. S6). Conventional



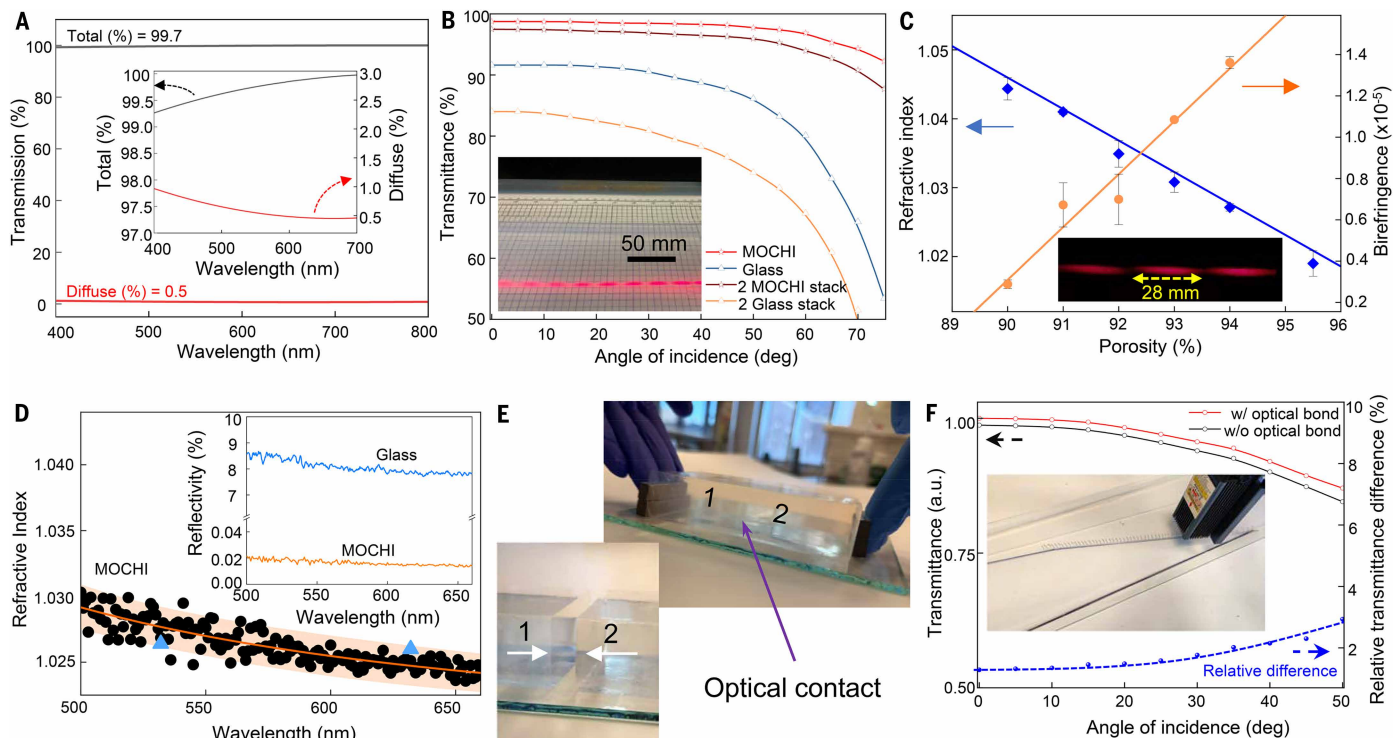


**Fig. 2. Optical properties of MOCHI.** (A) Total and diffuse transmission of 1-mm-thick MOCHI versus wavelength, showing a high average transparency of 99.7% with haze <1%. (Inset) Details of these dependencies. (B) Angular dependencies of transmittance for thin MOCHI films for single- and double-stacked MOCHI films as compared with glass counterparts, demonstrating >90% transmittance even at high incidence angles. (Inset) Laser light propagation through monocrystal-like monolithic MOCHI, with the periodic scattered light modulation arising from its birefringence properties. (C) Refractive index and birefringence versus porosity of MOCHI. Circular and diamond symbols indicate experimental data; the orange line is based on linear fitting. The refractive index dependence was fit (blue line) with a Arago-Biot relation averaging refractive indices of polysiloxane (1.457) and air (1.0003) at 632 nm, weighted by their volume fractions (24). (Inset) A zoomed-in view of modulated scattering laser light traversing through the metamaterial, on a dark background. (D) Variation of the average effective refractive index of MOCHI within the visible spectrum, derived from spectral reflectivity measurements. (Inset) Comparison of the spectral dependencies of reflectivity of MOCHI and glass. Blue triangles indicate the data points from independent measurements made by using laser light (24). (E) Photographs showing two 1-inch-thick MOCHI slabs achieving optical contact upon being pressed toward each other. Photographs were taken under illumination that was optimized to allow visibility of slabs that are generally “invisible” owing to weak surface reflections and transparency. (F) Normalized transmittance of MOCHI slabs in (E), before and after optical bonding for different incidence angles, indicating the relative transmittance improvement upon bonding. (Inset) Laser cutting multicentimeter-thick MOCHI slab placed atop glass, defining the shape printed on white underneath.

laser cutting (Fig. 2F, inset, and movie S7) allowed fabrication of multicentimeter-thick slabs of MOCHIs of arbitrary geometric shapes that could be invisibly tiled with other slabs through the creation of optical contacts (24).

The morphology of partially orientationally ordered polysiloxane nanotubes (Fig. 1, D to G) led to optical birefringence in the range of  $0.2 \times 10^{-5}$  to  $1.4 \times 10^{-5}$  (Fig. 2C and fig. S8), with the optical monocrystal-like ordering maintained over meter-scale dimensions of slabs defined by the directionality of solvent exchange and drying (24). Birefringence increased with porosity and showed a trend different from that of the effective refractive index (Fig. 2C).

Periodically modulated scattering of a laser beam traversing through the slab (Fig. 2, B and C, insets, and fig. S9A) vividly illustrates birefringence properties of these materials on large scales. The  $L_s \sim 2.5$  cm modulation period of scattered light corresponds to the beam’s polarization state changes from linear to circular (strong scattering) and back to linear (weak scattering) caused by the MOCHI’s macroscopic optical-monocrystal-like anisotropic properties. The phase difference between ordinary and extraordinary modes changed by  $\pi$  as the light traversed the distance corresponding to the  $\sim 2.5$ -cm-scale  $L_s$  (24), within which the beam’s polarization state changed from linear to circular (strong scattering) and back to linear (weak scattering). This birefringence is inconsequential for the main envisaged applications of MOCHI

as transparent thermal insulators but may find other applications, such as in polarizing optics. The very high visible-range optical transparency also yielded a high color rendering index >99% (24), so that viewing through MOCHI preserved natural colors (fig. S9B).

Mesoporous morphology was key to enabling the thermal properties of MOCHIs (Fig. 3A and figs. S10 to S12). Because the pores were much smaller than the mean free path between collisions of air molecules at ambient temperatures and pressures (60 to 70 nm), these molecules collide with the pore walls more often than with each other, so gas conduction of nanoconfined air was strongly inhibited. The tubular polysiloxane network of MOCHIs was also a poor thermal conductor because of its geometric complexity, poor thermal contacts at tubular junctions, and small solid fraction by volume.

The interplay between the conduction contributions caused by the gas and solid network was generally more complex than for conventional aerogels with polydisperse random pores because MOCHIs’ inner pores of tubes were monodisperse and small ( $\sim 5$  nm), whereas the 20- to 30-nm intertube pores were controlled by porosity (Fig. 1, C to H). These structural aspects may be a source of apparent two local minima on thermal conductivity versus porosity dependencies (Fig. 3A), although future studies will be needed to confirm this hypothesis. Furthermore, the polysiloxane within MOCHIs strongly absorbed radiation in most of the thermal infrared range that corresponds

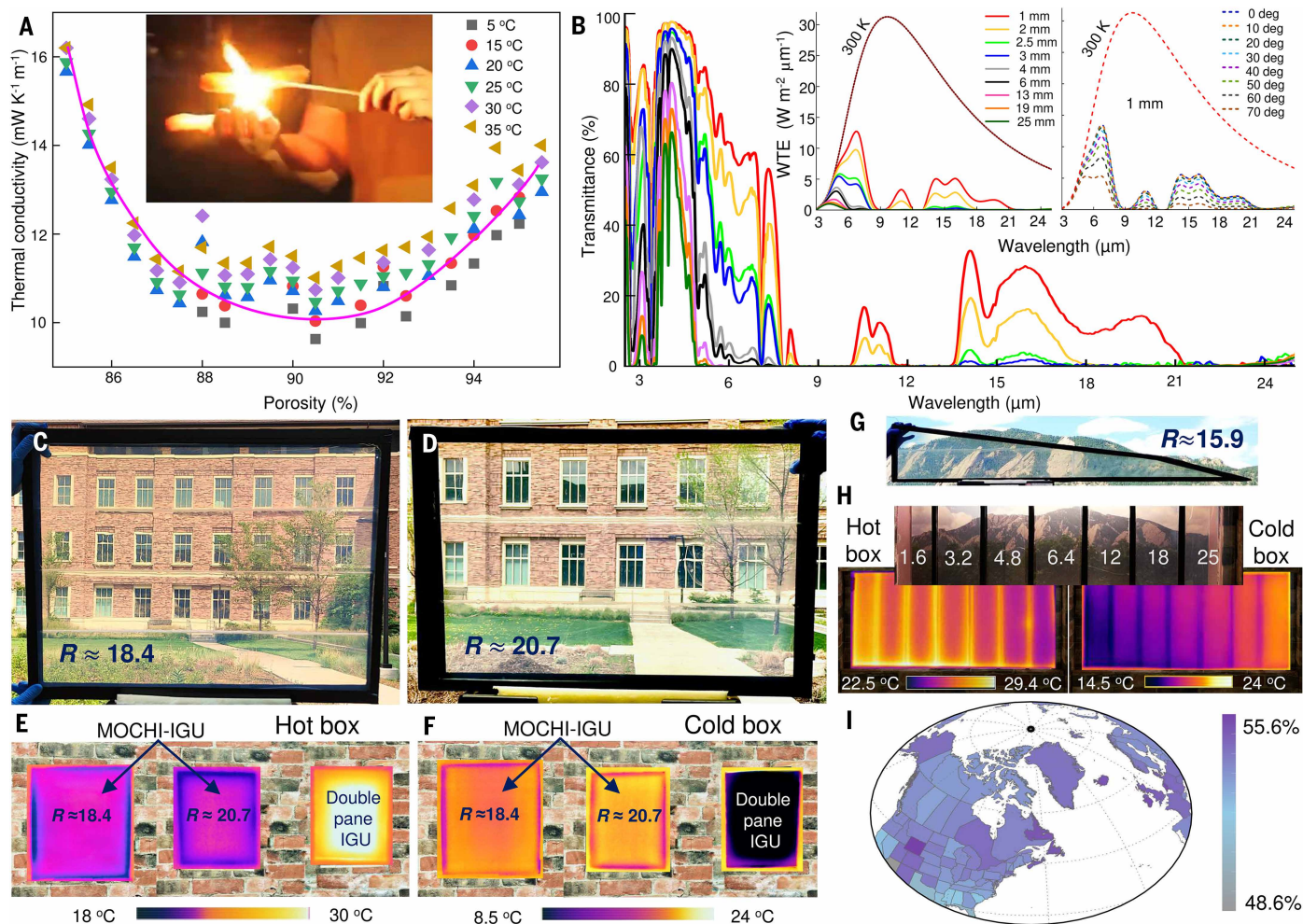


**Fig. 3. Thermal barrier properties and impact of using MOCHI in insulating glass units.** (A) Thermal conductivity of MOCHI versus porosity at different temperatures. The magenta solid line is an eye guide. (Inset) Photograph depicting the fire retardancy and thermal superinsulation of a MOCHI film while protecting from flame (movie S1), allowing for safe on-hand barbecuing. (B) Thermal infrared transmittance for MOCHI of varying thickness. (Insets) The weighted infrared transmissive emittance (WTE) per micrometer-unit wavelength (24) for blackbody radiation at 300 K, for MOCHI versus (left) thicknesses and (right) light's incidence angle for 1-mm-thick MOCHI. (C and D) Optical photographs illustrating high transparency and color rendering of MOCHI-IGUs. (C) 52.5 by 65 cm of 35 mm thickness with  $R \approx 3.24 \text{ m}^2 \text{ K W}^{-1}$  and (D) 35 by 50 cm of 37.5 mm thickness with  $R \approx 3.65 \text{ m}^2 \text{ K W}^{-1}$  (24), as measured for external and internal temperatures of  $-4^\circ$  and  $16^\circ\text{C}$ , respectively. (E and F) Thermal photographs of MOCHI-IGUs shown in (C) and (D) as compared with that of a conventional double-pane IGU with an air gap of 12 mm, in both (E) hot box (at  $40^\circ\text{C}$ ) and (F) cold box ( $-10^\circ\text{C}$ ) environments. (G) Optical photograph of a complex-shaped MOCHI-IGU with lateral dimensions 127.5 by 25 cm and thickness 37.5 mm having  $R \approx 2.8 \text{ m}^2 \text{ K W}^{-1}$  (24).  $R$  values marked in (C) to (G) are in  $\text{foot}^2\text{-hours } ^\circ\text{F Btu}^{-1}$ . (H) Optical and thermal images for MOCHI slabs with varying thickness, ranging from 1.6 to 25 mm, in which the latter were taken above hot and cold boxes at temperatures of  $40^\circ\text{C}$  and  $-10^\circ\text{C}$ , respectively. (I) Global map of percentage of a building's heating and cooling energy savings enabled by MOCHI-IGUs replacing single-pane windows, averaged over a year, as estimated for a standard single-family home (24).

to blackbody radiation at ambient conditions (Fig. 3B). Thus, the radiative contribution to heat transfer through thick slabs of MOCHI was negligible because sequential processes of absorption and reemission effectively led to thermal-range radiation bouncing back from the slab, which is consistent with our modeling of thermal resistance (fig. S13) and enabling high- $R$  insulating glass units (IGUs) with high visible-range transparency (figs. S14 to S18) (24).

Optimized-composition MOCHIs were highly insulating, with thermal conductivities of 10 to  $12 \text{ mW K}^{-1} \text{m}^{-1}$  at ambient temperatures (Fig. 3A) and thermal barrier properties useful for many applications (Figs. 3, C to I, and 4). MOCHIs also exhibited mechanical robustness (fig. S19 and movie S9) and could be adhered to plastic films or glass substrates, which allowed for undergoing hundreds of rolling-unrolling (fig. S20) and heating-cooling cycles (fig. S21), as well as accelerated lifetime characterization within an IGU or a retrofit (24). Because of

composition and large surface area of the mesoporous morphology, MOCHIs were fire retardant (Fig. 3A, inset, and movies S1 and S10), superhydrophobic, and water repellant (Fig. 1B, inset, and movie S6). These MOCHI properties persisted even after  $\sim 5$  years of being adhered to an interior surface of a window, under dust fouling, chemical exposure, and acid rain (figs. S21, E and F; S22; and S23) (24).

### Windows, skylights, and solar thermal energy harnessing

The thermal resistance of  $2.64 \text{ m}^2 \text{ K W}^{-1}$  ( $\approx 15 \text{ foot}^2\text{-hours } ^\circ\text{F Btu}^{-1}$ ) of optimized MOCHI of 2.5-cm slab thickness allowed for making window units that were insulated better than conventional building walls while having geometric form factors (thickness) comparable with that of the common double-pane windows (Fig. 3, C to I; figs. S14 to S18; and tables S3 to S5). Although relatively thin (3 mm) films of MOCHIs could be rolled and supercritically dried for applications in large-area



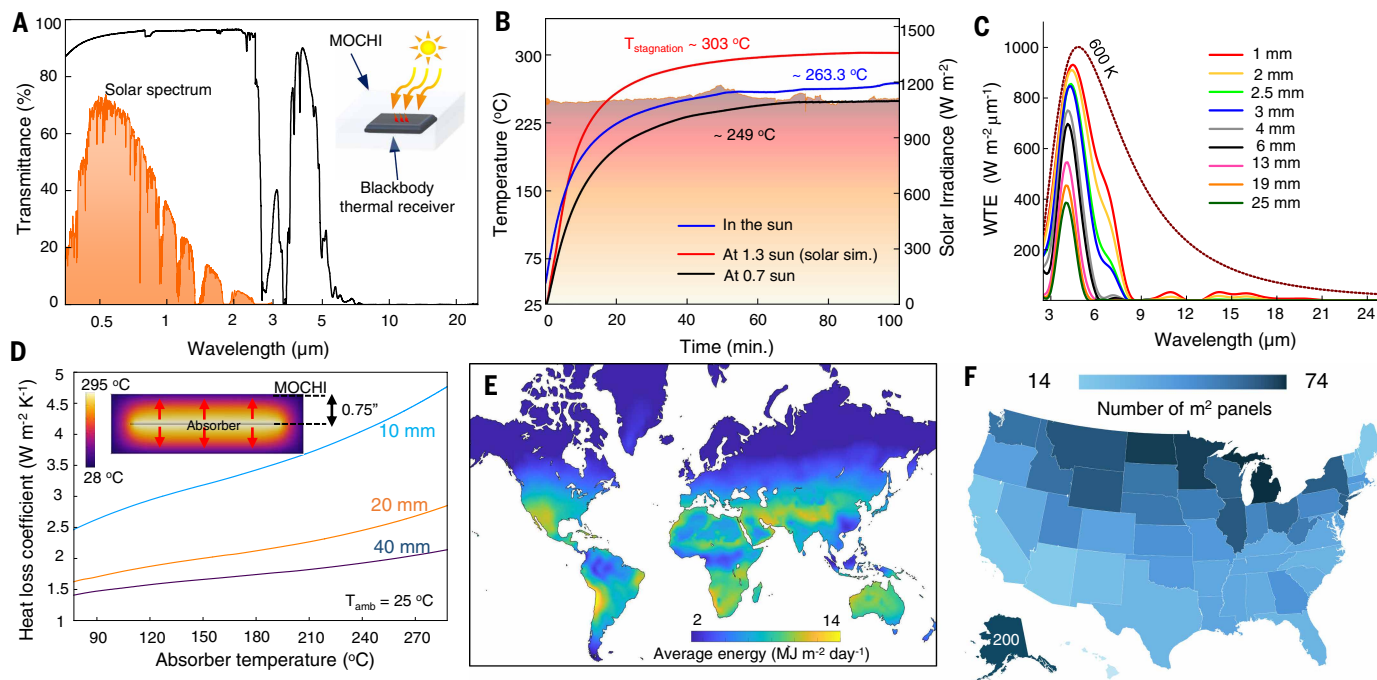


**Fig. 4. Solar thermal energy harnessing enabled with MOCHI.** (A) Spectral transmittance of a MOCHI slab (black curve) showing high transparency in visible and near-infrared ranges, which correspond to solar radiation spectrum (orange) at Earth's surface, along with strong absorption in the part of thermal infrared range  $>5\ \mu\text{m}$ . (B) Stagnation temperatures of a blackbody thermal receiver at various irradiation intensities obtained under ambient conditions (for monitored solar radiation intensity) and by using a solar simulator, as schematically shown in (A), inset (24). (C) The weighted transmissive emittance per micrometer-unit wavelength (24), weighted by 600 K blackbody radiation, for MOCHI slabs of different thicknesses. (D) Heat loss coefficient of the solar thermal harnessing system for MOCHI slabs of different thickness. (Inset) The heat escape from absorber through MOCHI. (E) Annual average energy generated by a solar thermal panel per square meter per day mapped throughout the world based on the average solar irradiation (24). (F) A map showing the number of square-meter panels required to meet heating and cooling energy needs for single-family homes in the United States, simulated with EnergyPlus according to the geographical location and average annual energy consumption (24).

window retrofits (Fig. 1A), scaling of thick slabs was challenging because the cost of vessels capable of operating at the elevated pressures of  $\text{CO}_2$ -based supercritical drying is prohibitive for large samples. However, the ability of forming good “optical contact” between edge faces of MOCHI slabs (Fig. 2, E and F, and movie S2) or large-area films allowed for scaling the size of high- $R$  MOCHI-IGUs made from overall laterally large and thick MOCHI slabs (Fig. 3, C to I). These slabs could be laser-cut to various geometric shapes (Fig. 2F, inset, and movie S7), providing the ability to make complex-shaped high- $R$  IGUs (Fig. 3G) (24).

Because MOCHIs effectively blocked thermal-range blackbody radiation under window-relevant conditions (Fig. 3B), high- $R$  thermal insulation could be achieved even without using low-emissivity coatings on glass (Fig. 3, C to I) (24), with experimentally measured  $R$  values matching the results of computational modeling (fig. S17 and table S5) (24, 25). However, 3- to 4-mm-thick MOCHI films adhered to the interior of single-pane windows boosted their insulation to be comparable with that of double-pane windows, with  $R \approx 0.53\ \text{m}^2\ \text{K}\ \text{W}^{-1}$  ( $3\ \text{foot}^2\text{-hours}\ ^\circ\text{F}\ \text{Btu}^{-1}$ ).

As an additional benefit beyond energy efficiency, the use of MOCHI in IGUs and retrofits also boosts condensation resistance (fig. S21A) and soundproofing (fig. S24) as compared with those of conventional single- and double-pane windows (24). IGUs with  $\approx 19$ - and 25-mm MOCHI slabs between panes reduced the sound transmission level by 25 to 35 dB within the 1- to 5-kHz frequency range and by 15 to 30 dB within the 0.5- to 1-kHz range, performing better than a conventional double-pane IGU by 5 to 10 dB within the entire studied range of sound frequencies.

Accelerated durability testing showed no detectable degradation, indicating an anticipated lifetime of at least 20 years (fig. S21B and

tables S6 and S7) (24), comparable with that of conventional IGUs. Because MOCHI can be confined between panes of glass, replacing air of conventional double-pane windows, or adhered to protective hard plastic films in retrofits, the window product durability was further enhanced by the glass or plastic confinement. However, even unprotected MOCHIs exhibit good durability under conditions expected for air-purifying disposable windows (fig. S23) (24). One of the reasons for selecting polysiloxane (silicone) in our MOCHI designs was that it is already widely used in edge sealing of commercial windows.

The combination of visible-range transparency and thermal insulation is of interest for many applications beyond windows. In one example (Fig. 4), we show how it allows for solar thermal energy harnessing, with the potential utility in compensating for the energy still leaking through building envelopes. By encasing a broadband blackbody solar absorber with our MOCHI, effectively transmitting solar but blocking thermal infrared radiation (Fig. 4A and figs. S25 and S26), we can entrap the absorbed solar thermal energy that can be then used for needs such as heating water or a building interior (Fig. 4, B to D). This energy harnessing yields high stagnation temperatures of  $\sim 300^\circ\text{C}$  as the absorber for both solar simulator and ambient conditions (Fig. 4B). At the high temperatures of a blackbody receiver, the blackbody radiation spectrum shifts to shorter wavelengths, at which MOCHIs become semitransparent (Fig. 4C and figs. S25 and S26). Therefore, differently from the ambient temperatures case, the radiative heat transfer becomes important at high stagnation temperatures of the blackbody receiver, causing some heat loss (Fig. 4D). Although one can modify MOCHIs to make them more opaque in the range of 3 to 6  $\mu\text{m}$  (fig. S26A) to further boost the solar thermal energy harnessing, the demonstrated stagnation temperatures (Fig. 4B) are the highest temperatures achieved

for unconcentrated solar radiation, to the best of our knowledge. The harnessed thermal energy can be channeled for heating a building interior or water by use of heat exchangers. Notably, harnessing can be done even on a cloudy day, when ambient solar energy is at  $\sim 0.3$  sun, which could be particularly advantageous in cold climates. Small parts of the opaque component of the building envelope could become solar heat-based power generators capable of reducing the overall building energy consumption (Fig. 4, E and F).

## Discussion

To assess the potential impact of using MOCHIs in building envelopes, we have performed EnergyPlus simulations to estimate the energy saving with the help of MOCHI-IGUs and solar thermal energy generation that could replace other energy sources used for heating and cooling the building interior, such as electricity and gas (24). The wall-grade efficient MOCHI-IGUs would allow for increasing the fraction of building envelopes occupied by windows, potentially boosting the window area to 30% from the current 8% while actually reducing the energy wasted for heating (Fig. 3I and figs. S27 and S28). The global variations of solar thermal energy generation per square meter of MOCHI-based solar thermal panel are shown in Fig. 4E and can be converted into interior-heating or solar thermal-powered cooling (26) energy or water heating. Typically, solar thermal panels covering a fraction of a single-family home's opaque envelope would be sufficient to meet the heating and cooling needs, as illustrated for US states in Fig. 4F. Having larger areas of solar thermal-harnessing panels would then generate energy beyond building's heating and cooling needs, converting it into an energy-generating plant.

We developed MOCHI metamaterials with high transparency and with thermal conductivity that is lower than that of still air, comparable with that of aerogels used in the Mars Rover (4–12). Cold-temperature insulation of MOCHI-IGUs stopped 95% of heat transfer, making windows as insulated as high-performing building walls. Self-assembly-based fabrication and optical-contact-enabled scaling of MOCHI slabs and films with diverse geometric form factors is suitable for applications in building envelopes. Our MOCHI can expand the use of insulated glazing in envelopes of future buildings, including in windows, skylights, and porous material-based daylighting (27, 28). Although silicone-based sealants are already widely used in IGUs, our MOCHI could replace the conventional gas fillers with “frozen air” nanosponge-like methyl-silicone-based fillers. Potential applications may extend to greenhouse coverings, protective and heat-insulating apparel (29), and space exploration (15), whenever simultaneous optical transparency and thermal insulation are needed. MOCHI can be surface-functionalized or modified by adding nanoparticles (30) to achieve custom-designed properties that range from solar gain control to air purification (31), potentially including disposable insulating air-cleaning windows (24).

## REFERENCES AND NOTES

1. F. Trubiano, Ed., *Design and Construction of High-performance Homes: Building Envelopes, Renewable Energies and Integrated Practice* (Taylor & Francis, 2013).
2. J. Lovell, *Building Envelopes: An Integrated Approach (Architecture Briefs)* (Princeton Architectural Press, 2010).
3. J. L. Aguilar-Santana, H. Jarimi, M. Velasco-Carrasco, S. Riffat, *Int. J. Low Carbon Technol.* **15**, 112–120 (2020).
4. I. I. Smalyukh, *Adv. Mater.* **33**, e2001228 (2021).

5. M. K. Carroll, A. M. Anderson, S. T. Mangu, Z. Hajjaj, M. Capron, *Sustainability (Basel)* **14**, 2887 (2022).
6. C. Buratti, E. Belloni, F. Merli, M. Zinzi, *Energy Build.* **231**, 110587 (2021).
7. E. Belloni, C. Buratti, F. Merli, E. Moretti, T. Ihara, *Energy Build.* **243**, 110999 (2021).
8. Q. Liu, I. I. Smalyukh, *Sci. Adv.* **3**, e1700981 (2017).
9. R. Hart, S. Selkowitz, C. Curcija, *Build. Simul.* **12**, 79–86 (2019).
10. T. Shimizu, K. Kanamori, A. Maeno, H. Kaji, K. Nakanishi, *Langmuir* **32**, 13427–13434 (2016).
11. E. Abraham et al., *Nat. Energy* **8**, 381–396 (2023).
12. Y. Kobayashi, T. Saito, A. Isogai, *Angew. Chem. Int. Ed.* **53**, 10394–10397 (2014).
13. L. Zhao et al., *Opt. Express* **27**, A39–A50 (2019).
14. Q. Liu et al., *Nano Energy* **48**, 266–274 (2018).
15. R. Wordsworth, L. Kerber, C. Cockell, *Nat. Astron.* **3**, 898–903 (2019).
16. B. Fleury et al., *ACS Appl. Mater. Interfaces* **12**, 34115–34121 (2020).
17. C.-S. Ha, S. S. Park, *Periodic Mesoporous Organosilicas: Preparation, Properties and Applications*, *Springer Series in Materials Science*, vol. 281 (Springer, ed. 1, 2019).
18. C. T. Kresge, M. Leonowicz, W. J. Roth, J. C. Vartuli, J. S. Beck, *Nature* **359**, 710–712 (1992).
19. K. M. McGrath, D. M. Dabbs, N. Yao, I. A. Aksay, S. M. Gruner, *Science* **277**, 552–556 (1997).
20. C. P. Singh et al., *Appl. Phys., A Mater. Sci. Process.* **77**, 585–589 (2003).
21. S. H. Tolbert, A. Firouzi, G. D. Stucky, B. F. Chmelka, *Science* **278**, 264–268 (1997).
22. K. M. McGrath et al., *Langmuir* **16**, 398–406 (2000).
23. M. Kruk, M. Jaroniec, V. Antochshuk, A. Sayari, *J. Phys. Chem. B* **106**, 10096–10101 (2002).
24. Materials and methods are available as supplementary materials.
25. R. Mitchell et al., *WINDOW 7 User Manual* (Lawrence Berkeley National Laboratory, 2019); <https://windows.lbl.gov/window-documentation>.
26. C. A. Balaras et al., *Renew. Sustain. Energy Rev.* **11**, 299–314 (2007).
27. M. Ganobjak et al., *J. Build. Eng.* **64**, 105600 (2023).
28. K. McEnaney, L. Weinstein, D. Kraemer, H. Ghasemi, G. Chen, *Nano Energy* **40**, 180–186 (2017).
29. F. Azam et al., *Adv. Mater. Sci. Eng.* **2022**, 1 (2022).
30. Q. Liu, H. Mundoor, G. H. Sheetah, I. I. Smalyukh, *Opt. Express* **28**, 34237–34245 (2020).
31. S. Hu et al., *Environ. Sci. Nano* **11**, 4666–4691 (2024).

## ACKNOWLEDGMENTS

We thank B. Borak, K. Burrows, J. Cameron, J. De La Cruz, T. Culp, C. Fitz, J. Gerbi, A. Hess, M. Krarti, M. Lafrance, Q. Liu, P. de Melo, S. Mummé, E. Schiif, M. Sofos, R. Tenent, T. White, and Y. Yuan for discussions. We are grateful to F. Leresche for discussions and the use of a solar simulator, as well as H. Zhao and R. Fei for technical assistance. **Funding:** We acknowledge support of the US Department of Energy (DOE), under the Advanced Research Projects Agency–Energy (ARPA-E) award DE-AR0000743, during which the development of MOCHIs was initiated (J.B.t.H., E.A., V.C., B.S., T.L., B.F., and I.I.S.). We also acknowledge the DOE EERE grant DE-EE0009699 that supported the development of thick slabs of MOCHI and highly insulating glass units based on them (A.B., E.A., B.S., T.L., and I.I.S.). We acknowledge the CU BEST center for the partial support of solar thermal energy harnessing part of this work (A.B. and I.I.S.). **Author contributions:** A.B., B.F., B.S., E.A., J.B.t.H., T.L., and V.C. contributed equally and are listed in the byline in alphabetical order by first name. Conceptualization: I.I.S. Methodology: A.B., B.F., B.S., E.A., J.B.t.H., T.L., V.C., I.I.S. Investigation: A.B., B.F., B.S., E.A., J.B.t.H., T.L., V.C., I.I.S. Funding acquisition: I.I.S. Project administration: I.I.S. Supervision: I.I.S. Writing – original draft: A.B., B.S., E.A., J.B.t.H., T.L., I.I.S. Writing – review & editing: A.B., B.F., B.S., E.A., J.B.t.H., T.L., V.C., I.I.S. **Competing interests:** The authors filed US patent applications related to MOCHI technology (patent no. US 12,241,305 B2); additional patent applications were filed concurrently with the submission of this manuscript (application nos. 63/811,412 and 63/812,787). **Data and materials availability:** All data are available in the main text or in the supplementary materials. Information requests should be directed to the corresponding author. **License information:** Copyright © 2025 the authors, some rights reserved; exclusive licensee American Association for the Advancement of Science. No claim to original US government works. <https://www.science.org/about/science-licenses-journal-article-reuse>

## SUPPLEMENTARY MATERIALS

[science.org/doi/10.1126/science.adx5568](https://science.org/doi/10.1126/science.adx5568)

Materials and Methods; Supplementary Text; Figs. S1 to S28; Tables S1 to S7; References (32–62); Movies S1 to S10

Submitted 19 March 2025; resubmitted 6 May 2025; accepted 8 October 2025

[10.1126/science.adx5568](https://science.org/doi/10.1126/science.adx5568)